Silicon (2021) 13:451–465
https://doi.org/10.1007/s12633-020-00454-w

ORIGINAL PAPER

Design, Facile Synthesis and Characterization of Porphyrin-Zirconium-Ferrite@SiO_2 Core-Shell and Catalytic Application in Cyclohexane Oxidation

Hamideh Balooch Khosravi[1] · **Rahmatollah Rahimi**[1] · **Mahboubeh Rabbani**[1] · **Ali Maleki**[1] · **Afsaneh Mollahosseini**[1]

Received: 25 September 2019 / Accepted: 12 March 2020 / Published online: 21 March 2020

Abstract

In this study, a new magnetic $ZrFe_2O_4@SiO_2$-TCPP nanocatalyst with high efficiency was used for the oxidation of cyclohexane to cyclohexanone (Ke) and cyclohexanol (Al). The mesoporous $ZrFe_2O_4$ nanoparticles, with a nanocauliflower structure was synthesized via solvothermal method and it was coated with SiO_2 sell by tetraethyl orthosilicate (TEOS) to fabricate the $ZrFe_2O_4@SiO_2$ core-shell. Then, this composite was modified by 5, 10, 15, 20-meso-tetrakis(4-carboxyphenyl) porphyrin (TCPP). FT-IR, XRD, XPS, FE-SEM, EDX, TEM, VSM, BET and fluorescence analyses were used to characterize the prepared nanomaterials. Optimization of the reaction conditions, as one of the most applicable Response Surface Methodologies (RSM), was executed by Central Composite Design (CCD) based on the applied mathematical modeling, and the results were analyzed by GC-Mass Analytical Testing Lab Services. The maximum Ke/Al products were 33.6 and 18.9%, respectively. Simple separation by a magnetic field, stability and recoverability, are the advantages of this new catalyst.

Keywords Magnetic nanoparticles · Zirconium-ferrite · Mesoporous · Core-shell · TCPP · Oxidation · Cyclohexane

1 Introduction

Products derived from cyclohexane oxidation such as cyclohexanone (Ke) and cyclohexanol (Al) are important products because there are high demands for them. They are also important as raw materials for producing adipic acid and caprolactam [1].These two raw material used in the production of fibers, nylon-6,6, food additives, and plasticizers are manufactured by the oxidation of cyclohexanone, obtained either by hydrogenation of phenol or, more commonly, by the oxidation of cyclohexane [2–4].

The liquid-phase aerobic oxidation of cyclohexane to a mixture of cyclohexanol and cyclohexanone, known as KA oil has always been an area of intensive research [5–7] because it is one of the key steps in the industrial production of caprolactam and nylon [3, 8]. For this particular alteration, current industrial methods either employ cobalt salts as catalysts or use no catalyst at all (autoxidation at a higher temperature). However, there are several significant deficiencies associated with the current technology, such as low conversion (~4%) and low selectivity for the eligible product (<80%). Thus, the industrial production of K/A oil from cyclohexane has been considered a process of low efficiency [6, 8].

In the search for alternative pathways to produce chemical precursors, the use of stoichiometric oxidants and catalysts has been studied. In this context, heterogeneous catalysts and molecular oxygen as an oxidant have received attention in the last several years because heterogeneous semiconductor materials allow for chemical conversions using visible light irradiation as an energy source under ambient pressure and temperature conditions [9, 10].

The heterogeneous catalytic oxidation reactions are proposed as viable methods due to the stability, *recoverability, and reusability* of the catalyst, which are still a challenge in sustainable chemical processes development. The loading of the catalyst on magnetic materials such as ferrites has been proposed as an artificial procedure that makes this issue critical in chemistry [11–13].

✉ Rahmatollah Rahimi
Rahimi_rah@iust.ac.ir

✉ Ali Maleki
maleki@iust.ac.ir

[1] Department of Chemistry, Iran University of Science and Technology, Tehran 16846-13114, Iran

There are several approaches for the synthesis of ferrites such as microwave [14], solvothermal [15], mechanochemical [16], sonochemical [16], and wet chemical methods [17]. Recently, solvothermal reaction, a high-pressure route, is attended for preparing nano ferrites in mild temperature conditions [18]. In this work, the $ZrFe_2O_4$ ferrite was synthesized by using the solvothermal method as the core. The structure of $ZrFe_2O_4$ is the same as distribution models of Fe^{2+}, Fe^{3+}, and Ti^{4+} ions in $TiFe_2O_4$ because Zr is one of the family groups of Ti [19].

On the other hand, the coating of magnetic nanoparticles with various materials such as metal oxides, noble metals, and polymers improves the performance of magnetic nanoparticles in different applications. For example, it provides a situation for organic molecules to attach to MNPs surface by covalent bonds. Due to the resistance of silica (SiO_2) against the degradation, it is recognized as the best and efficient surface functionalization [1, 20, 21]. The silica shell on the surface of ferrite nanoparticles, not only protects the magnetic cores from aggregating but also enables new functional groups immobilization. TEOS, as an excellent system for uniform coating on nanomagnetic particles, can be hydrolyzed to silica particles by ammonia (pH = 10–12) [22].

In this study, magnetic $ZrFe_2O_4$ nanoparticles were coated with SiO_2 as the shell, then modified by 5,10,15,20-meso-tetrakis(4-carboxyphenyl) porphyrin (TCPP) to fabricate a novel magnetic heterogeneous $ZrFe_2O_4@SiO_2$-TCPP nanocomposite as a catalyst.

Porphyrins are known as attractive compounds in chemical science because of its heterocyclic building blocks with a highly π-conjugated system. It has considerable catalytic properties due to their exciting chemical and photochemical characteristics. The meso position of the porphyrin is one of the most reactive centers; the substituent effect on the electrochemical property of porphyrins that influence the efficiency of catalytic and electron transfer processes [23, 24]. TCPP is a kind of porphyrin, consists of a porphin and four benzoic acid groups. These macromolecules can be linked to magnetic materials [25], as well as to influence the electron transfer of porphyrins [26–31].

Therefore, by these capabilities, porphyrins play an essential role in the oxidation of alcohols, sulfides, and epoxidation of alkenes and alkanes and as a photosensitizer [32, 33]. These biomolecules have excellent performance in cyclohexane oxidation. Therefore, $ZrFe_2O_4@SiO_2$-TCPP nanocomposite was applied to cyclohexane oxidation under refluxing conditions and natural light in CH_3CN as a solvent. The products (Ke and Al) were evaluated by gas chromatography–mass spectrometry (GC-MS).

The statistically essential variables of the process were evaluated and optimized using the response surface methodology (RSM) based on the central composite design (CCD) [34–37] which is used by Design of Experiments (DoE) software; it is a statistical powerful tool for optimizing processes. The most significant advantage of DoE software is the ability to quickly detect how interactions between factors can affect production efficiency and quality [38]. The results obtained from DoE are analyzed to find which factors influence the results in a statistically relevant manner and which of those are interdependent.

Variables like catalyst amount, oxidant amount, and time of the oxidation process were evaluated and optimized. The characterizations of prepared materials were performed by Fourier transform infrared (FT-IR) spectroscopy, X-ray diffraction (XRD), X-ray photoelectron spectrometry (XPS), field emission scanning electron microscopy (FE-SEM), transmission electron microscopy (TEM), energy dispersive spectroscopy (EDS), nitrogen adsorption and desorption isotherms Brunauer-Emmett-Teller (BET), vibrating sample magnetometer (VSM), fluorescence and gas chromatography mass spectroscopy (GC-MS) techniques.

2 Experimental Section

2.1 Chemicals and Equipment

In this study, iron (III) chloride ($FeCl_3.6H_2O$), zirconium chloride ($ZrCl_4$), ammonium acetate ($NH_4CH_3CO_2$), ethylene glycol ($C_2H_6O_2$), ethanol (C_2H_5OH) 96% and 99%, dry toluene (C_7H_8), tetraethylorthosilicate (TEOS), cyclohexane, tert-butyl hydroperoxide (TBHP), acetonitrile, pyrrole, propionic acid, 4-carboxybenzaldehyde, solvents, and reagents were purchased from Merck and Aldrich and have been used without any further purification.

The functional groups of the materials were recorded by Fourier transform infrared spectroscopy (FT-IR) on a Shimadzu FTIR 8400S spectrophotometer with KBr pellet. X-ray diffraction (XRD) analysis was performed on Philips Pw 1730 X-ray diffractometer with Cu Kα radiation. X-ray photoelectron spectrometry (XPS) measurements were carried out with a monochromatic Al Kα (hν = 1486.6 eV) 240 W X-ray source and base pressure was 10^{-10} mbar which is equipped by Germany Bestec. Company and all of the spectra were calibrated to the binding energy of the adventitious C 1 s peak at 284.8 eV.

The morphology of the synthesized samples was observed by a Tescan Mira3 field emission scanning electron microscopy (FE-SEM). Transmission electron microscopy (TEM) was done to determine the particle size by Philips CM30. The elemental constituents of samples were obtained by energy-dispersive X-ray spectroscopy (EDX) using VEGAII, Tescan, Czech Republic instruments. The nitrogen (N_2) adsorption and desorption equipment, Brunauer-Emmett-Teller (BET) surface areas and Barrett-Joyner-Halenda (BJH) pore sizes were calculated on an ASAP 2020 (Micromeritics Ins. Corp.) at liquid nitrogen. Vibrating sample magnetometer

(VSM, MDKB, Magnetic Daghigh Kavir Co. Iran) was also employed to measure the magnetic behavior of nanomagnetic particles at room temperature. Spectrofluorophotometer (RF-6000, Shimadzu) was used to characterize the optical properties of materials, for GC-MS was used a PerkinElmer Clarus 680 GC equipped coupled to a PerkinElmer Clarus SQ 8 S mass spectrometer.

2.2 Synthesis of Mesoporous $ZrFe_2O_4$ Nanocauliflowers

First, 4 mmol (1.082 g) $FeCl_3.6H_2O$ and 2 mmol (0.466 g) $ZrCl_4$ were dissolved in 70 mL ethylene glycol under vigorous stirring at 600 rpm for 20 min to form a clear solution. Then, 30 mmol (2.312 g) $NH_4CH_3CO_2$ as a protective agent was added into the mixture solution under an ultrasonic bath for 30 min to form a dark yellow solution. Then, it was vigorously stirred at 600 rpm for 30 min at room temperature. Next, the mixture was sunk in a 100 mL Teflon-line stainless steel autoclave, fixed and kept in at 210 °C for 48 h. It was allowed to cool down at room temperature. As a result, the black precipitate was collected by an external magnetic field and washed with distilled water and ethanol several times. Finally, the product was dried in a vacuum system at 60 °C for 12 h [15].

2.3 Synthesis of $ZrFe_2O_4@SiO_2$ Nanocomposite

$ZrFe_2O_4@SiO_2$ is obtained by modifying the Stober method [22]. Typically, 45 mg as-prepared $ZrFe_2O_4$ nanocauliflowers were dispersed in the mixture of (80 mL) ethanol and (16 mL) distilled water in an ultrasonic bath for 20 min. Then (2 mL) NH_4OH was slowly added under vigorous magnetic stirring for 30 min (pH = 11). Next, (0.8 mL) TEOS was dropped-wise added to the above mixture under vigorous stirring at room temperature for 2 h. Finally, it was washed with ethanol and distilled water for three times. The products were dried at 60 °C for 12 h in a vacuum oven.

2.4 Synthesis of $ZrFe_2O_4@SiO_2$-TCPP Nanocomposite

TCPP was prepared according to previous literature [39]. 0.2 g $ZrFe_2O_4@SiO_2$ nanocomposite was dispersed in 80 mL in DMF by the ultrasonic bath. 0.04 g TCPP was added to the mixture and refluxed in 150 °C for 8 h. Finally, it was washed with ethanol and distilled water and dried in a vacuum oven [40] (Scheme 1).

2.5 Oxidation of Cyclohexane by Central Composite Design (CCD)

In the following experiments, the efficiency of the oxidation process of cyclohexane to produce cyclohexanone and cyclohexanol was evaluated under different operational variables utilizing Response Surface Methodology (RSM) based on Central Composite Design (CCD) [34]. The reaction condition is 10 mmol cyclohexane, 2–11% $ZrFe_2O_4@SiO_2$-TCPP (as catalyst), 5-11 mmol TBHP (as oxidant), and 10 mL acetonitrile (as the solvent) for 0–80 min under refluxing conditions.

3 Results and Discussion

3.1 FT-IR Spectra of the Prepared Samples

FT-IR spectra of A) $ZrFe_2O_4$, B) $ZrFe_2O_4@SiO_2$, and C) $ZrFe_2O_4@SiO_2$-TCPP are shown in Fig. 1. Peaks at 585 and 455 cm^{-1} belong to Fe-O and Zr-O bands, respectively. The peaks at 3444, 1645 and 1398 cm^{-1} point out the presence of O-H stretching, bending and deforming vibration of adsorbed water [3]. At spectrum of $ZrFe_2O_4@SiO_2$, the new sharp peaks at 1090, 800 and 420 cm^{-1} assigned to the asymmetry stretching, symmetric stretching and bending vibrations of Si-O of the silica shell on the $ZrFe_2O_4$ nanocauliflowers [14, 41].

In spectra of $ZrFe_2O_4@SiO_2$-TCPP, the presence of the peak at 3200 cm^{-1} approve N-H bending vibration band of pyrrole ring and at 2900 cm^{-1} show the C-H stretching vibration of aryl group which corresponds to FT-IR spectrum of TCPP. Referring to the FT-IR spectrum of pure TCPP, a sharp C=O stretching peak can be observed at 1700 cm^{-1} [42], but after the TCPP molecules were chemically fixed on $ZrFe_2O_4@SiO_2$, the intensity of C=O peak significantly decreased and appeared at 1635 cm^{-1} [33, 42–44].

3.2 Structural Characterization of the Prepared Samples

Figure 2 shows the XRD patterns of $ZrFe_2O_4$, $ZrFe_2O_4@SiO_2$ and $ZrFe_2O_4@SiO_2$-TCPP. It confirms that all the samples were formed in an inverse spinel structure similar to that of the magnetite (space group Fd3m, No. 227, with standard card JCPDS No. 01–088-0315). The Fe^{+2}, $Fe^{+3}$and Zr^{+4} ions were allocated into both the tetrahedral and octahedral void of magnetite phase [45]. According to the Debye–Scherrer formula, the crystallite size of the sample is given by:

$$D = 0.9\lambda/\beta\cos\theta$$

Where β is the full-width at half-maximum (FWHM) value of XRD diffraction lines, the wavelength $\lambda = 0.154056$ nm and θ is the half diffraction angle of 2θ. The crystallite size of $ZrFe_2O_4$ nanocauliflowers was found 44.6 nm, which calculated by taking the average of the size at its peaks. In conclusion, Zr^{4+} ions occupy both the interstitial sites (tetrahedral and octahedral) by

Scheme 1 Synthesis prosses of $ZrFe_2O_4@SiO_2$-TCPP

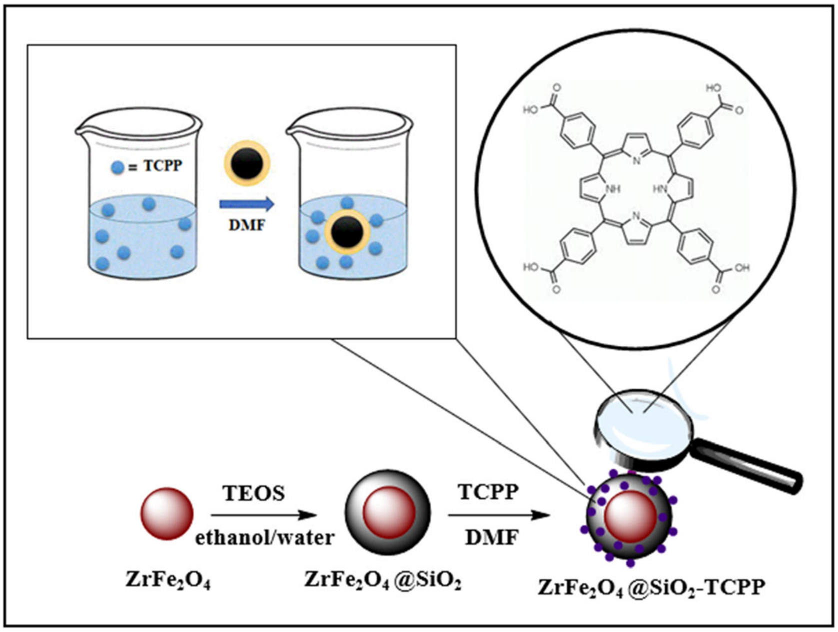

substituting Fe^{3+} ions of the spinel structure, which have also been reported earlier [46]. The ionic radii of Zr^{4+} and Fe^{3+} are different, led to the difference in their substitution behavior such as lattice parameter and magnetic properties [19].

The intensity of the peaks was decreased after modification, which was attributed to the silica shell enwrapped on the surface of particles. No extra peaks for other phases were detected in this pattern and no redundant reaction occurred between the core, and shell.

The crystallite size of $ZrFe_2O_4$, $ZrFe_2O_4@SiO_2$, and $ZrFe_2O_4@SiO_2$-TCPP based on Scherrer equation was 41.3, 36.9, and 26.5 nm, respectively, indicated that after coating of ferrite with SiO_2, and modifying by the TCPP crystallite size of nanostructures were decreased.

3.3 X-Ray Photoelectron Spectrometry (XPS)

$ZrFe_2O_4$ was further analyzed by XPS to determine the distribution of the elements and oxidation degrees on the surface of the sample. Figure 3 displays the XPS survey spectra of Fe2p, Zr3d, and O1s centered at 711, 182, and 530 eV, respectively.

As shown in Fig. 4, the Fe 2p XPS spectra contained iron revealed the presence of three types of Fe on the surface sample. Fe (II) and Fe (III) oxidation states are characterized at 709.3 and 711.2 eV, respectively. A significant shoulder at 713.9 eV is attributed to Fe in bond with oxygen and zirconium, which is a characteristic peak for a non-stoichiometric oxide [47].

The Zr 3d XPS spectra (Fig. 5) showed the exiting of Zr^{4+} on the surface of the sample because of $Zr3d_{3/2}$, and $Zr3d_{5/2}$

Fig. 1 The FT-IR spectra of the prepared samples (A: $ZrFe_2O_4$, B: $ZrFe_2O_4@SiO_2$ and C: $ZrFe_2O_4@SiO_2$-TCPP)

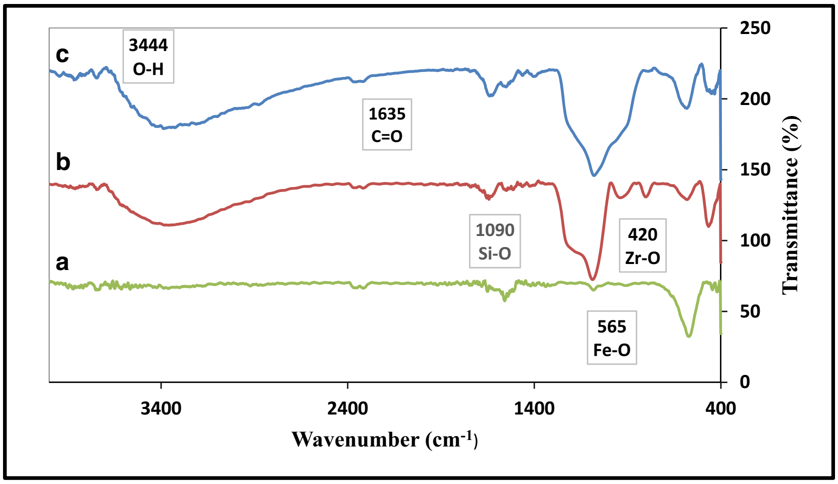

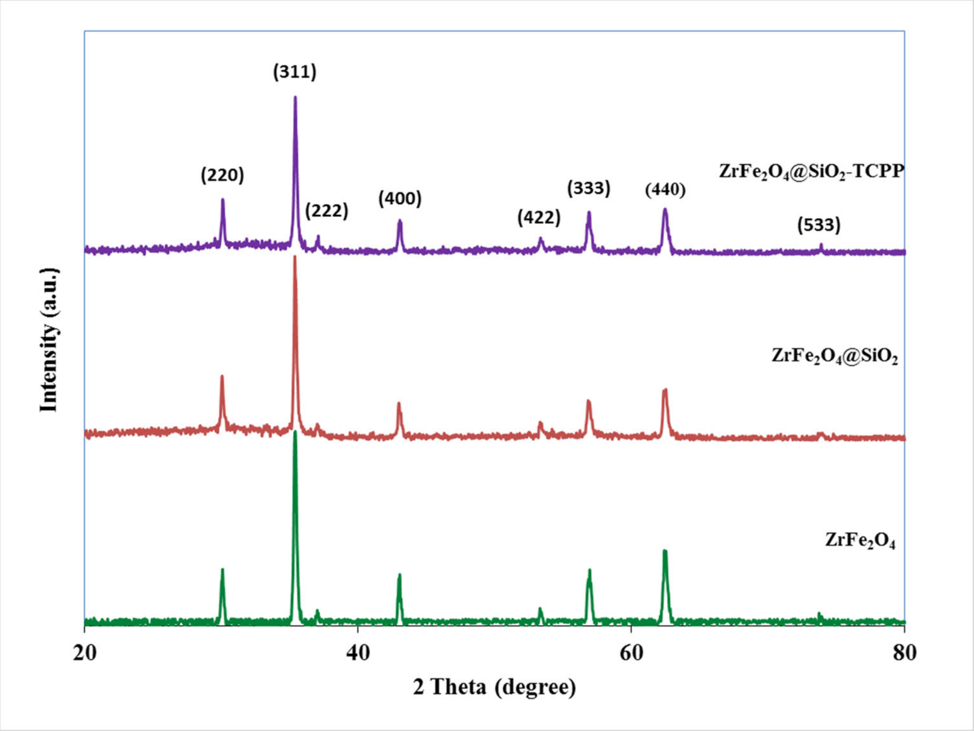

Fig. 2 The XRD pattern of the prepared samples

peaks were observed at a binding energy of 182.4, and 184.7 eV, respectively [48, 49].

Moreover, the types of surface oxygen species were identified by the O1s XPS spectra, as displayed in Fig. 6. It can be seen that the O1s curves of the mixed oxides can be fitted into four peaks. The binding energies and relative fractions listed in Table 1. Accordioning to literature [50, 51], the peak at 528.6 eV is ascribed to lattice oxygen atoms in a bond with Zr and the peak at 529.9 eV is ascribed to lattice oxygen atoms in a bond with Zr; a sharp peak O_{III} at 531.4 eV is assigned to oxygen vacancies, surface adsorbed oxygen ions or OH groups; another peak O_{IV} at 534.3 eV is likely to be associated with adsorbed molecular water.

3.4 Morphological Characterization of the Prepared Samples

The microstructure of the samples can be identified by scanning electron microscope (SEM, EDX mapping) tool. Figure 7a-c indicate that $ZrFe_2O_4$ particles have been fabricated at nano size with regular shapes. Very fine $ZrFe_2O_4$ particles with an average size of 35 nm were agglomerated to form

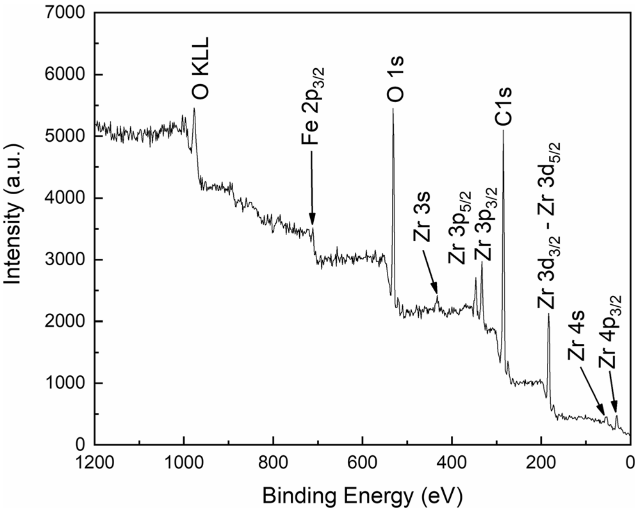

Fig. 3 XPS survey spectra of $ZrFe_2O_4$ sample

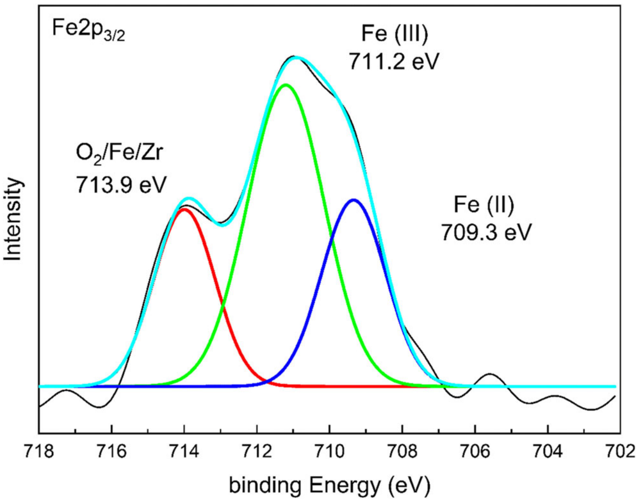

Fig. 4 The Fe 2p XPS spectra of $ZrFe_2O_4$

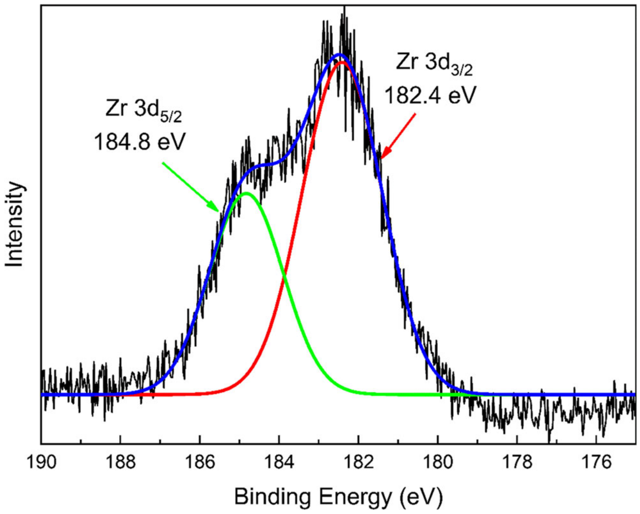

Fig. 5 The Zr 3d XPS spectra of $ZrFe_2O_4$

nanocauliflowers with an average size of 150 nm. SEM images of prepared nanocomposites indicate that following to SiO_2 coating and functionalizing (with TCPP), the average size of nanoparticles decreased to 32 and 29 nm for $ZrFe_2O_4@SiO_2$ and $ZrFe_2O_4@SiO_2$-TCPP, respectively. Probably, it may occur due to the ultrasonic bath before immobilization of SiO_2 and porphyrin. Figure 7d-f shows EDX mapping of samples, which (D) indicated the Zr, Fe and O in the core of the composite and Fig. 7e, f shows the presence of a layer of silica particles on the ferrite.

Figure 8 shows the typical TEM images of the $ZrFe_2O_4@SiO_2$-TCPP nanocomposite, which indicates a well-defined core-shell mesoporous nanostructure. Ethylene glycol and ammonium acetate play essential roles in the self-assembly of the nanocrystals and fabrication of monodisperse fine metal oxides [52]. On the other hand, the acetate ions absorb on the surface of the excellent size nanocrystals of Zr ferrite (about 6 nm) that inhibit the further growth of nanocrystals (Fig. 9). The surface energy of these tiny subunits is too high. To reduce their surface, spherical energy aggregation should happen through a strong surface tension force. The force of electrostatic repulsion and surface tension, balance to form of mesoporous $ZrFe_2O_4$ nanocauliflowers [53].

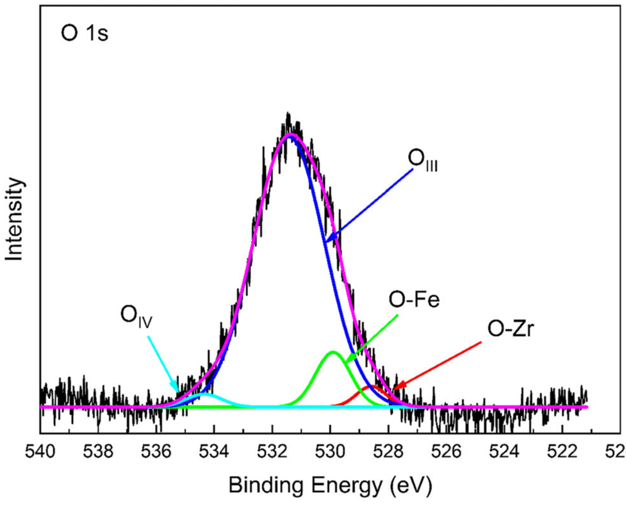

Fig. 6 The O1s XPS spectra of $ZrFe_2O_4$

Table 1 The binding energies and relative fractions for O1s, Fe2p3/2, and Zr $3d_{3/2}$ of the XPS spectra of $ZrFe_2O_4$

Type	Binding Energy (eV)	Area	FWHM	Fraction (%)
Lattice Oxygen-Zr	528.6	43.3	1.2	3
Lattice Oxygen -Fe	529.9	134.8	1.4	9
O_{III}	531.4	1352.1	2.9	85
O_{IV}	534.3	32.6	1.4	3
Fe (II)	709.3	91.7	2.0	26
Fe (III)	711.2	178.7	2.5	50
O_2/Fe/Zr	713.9	83.2	1.9	24
Zr $3d_{3/2}$	182.4	483.7	2.4	64
Zr $3d_{5/2}$	184.8	270.0	2.2	36

3.5 Elemental Analysis of $ZrFe_2O_4$ and $ZrFe_2O_4@SiO_2$

The elemental composition of mesoporous $ZrFe_2O_4$ nanocauliflowers and $ZrFe_2O_4@SiO_2$ obtained using energy-dispersive X-ray spectroscopy (EDX). As be seen in Fig. 10, EDX pattern of $ZrFe_2O_4$ nanocauliflowers shows the peaks of Fe, Zr, Si and O elements and approved the presence of iron and zirconium in the molar ratio of 2:1. These results confirmed the existence of SiO_2 on the $ZrFe_2O_4$ surface. Furthermore, the molar ratio of SiO_2 to $ZrFe_2O_4$ was 10:1, which confirmed by the XRF analysis of samples.

3.6 Nitrogen Adsorption and Desorption Isotherms of $ZrFe_2O_4$ and $ZrFe_2O_4@SiO_2$-TCPP

The specific surface area and pore volume data of the mesoporous $ZrFe_2O_4$ nanocauliflowers and $ZrFe_2O_4@SiO_2$-TCPP composite were characterized using the N_2 sorption method, with a typical isotherm shown in Fig. 11 Data obtained by BET demonstrated type IV isotherms, also showed large surface areas for the $ZrFe_2O_4$ and $ZrFe_2O_4@SiO_2$-TCPP composite (431 and 978 m^2g^{-1}, respectively). These values are relatively large compared to other reported mesoporous ferrite structures [54]. The uniform pore sizes of the $ZrFe_2O_4$ and $ZrFe_2O_4@SiO_2$- TCPP were found to be 5.8635 and 4.5345 nm, respectively. The decreasing particle size of composite rather than pure ferrite can lead to the decrease of pore size and increase of surface area and pore volume of the nanocomposite. The pore volume of $ZrFe_2O_4$ and $ZrFe_2O_4@SiO_2$- TCPP composite were calculated 0.5812 and 0.9692 cm^3/g, respectively. The

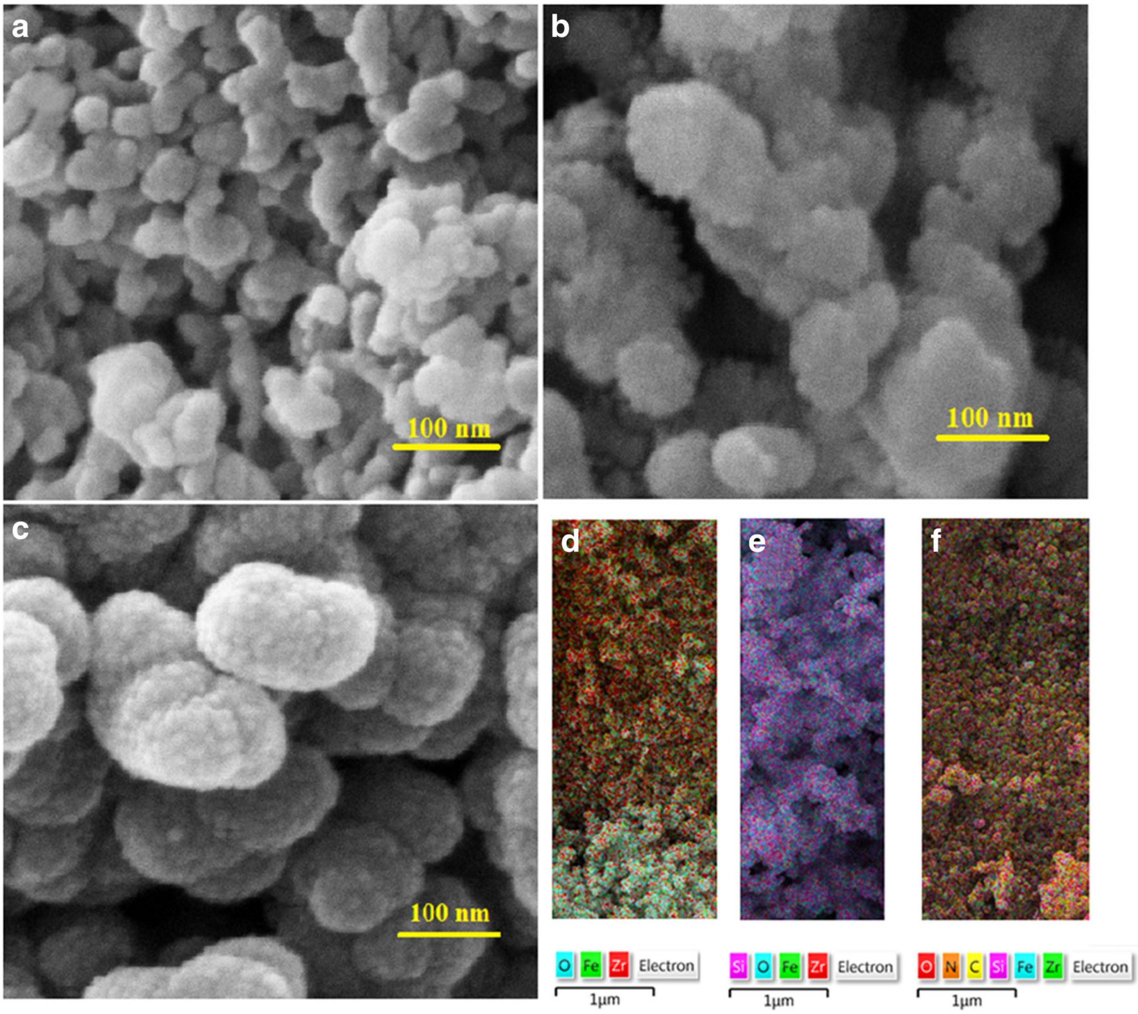

Fig. 7 The SEM images and EDX mapping of (**a**, **d**) $ZrFe_2O_4$, (**b**, **e**) $ZrFe_2O_4@SiO_2$ and (**c**, **f**) $ZrFe_2O_4@SiO_2$-TCPP

$ZrFe_2O_4@SiO_2$-TCPP composite showed higher textural mesoporosity, volume that facilitates the achievement in its area of the scaffold-confined mesoporosity, and modifying its catalytic properties.

3.7 Magnetic Properties of the Prepared Samples

The magnetic properties of mesoporous $ZrFe_2O_4$ nanocauliflowers were measured at room temperature by

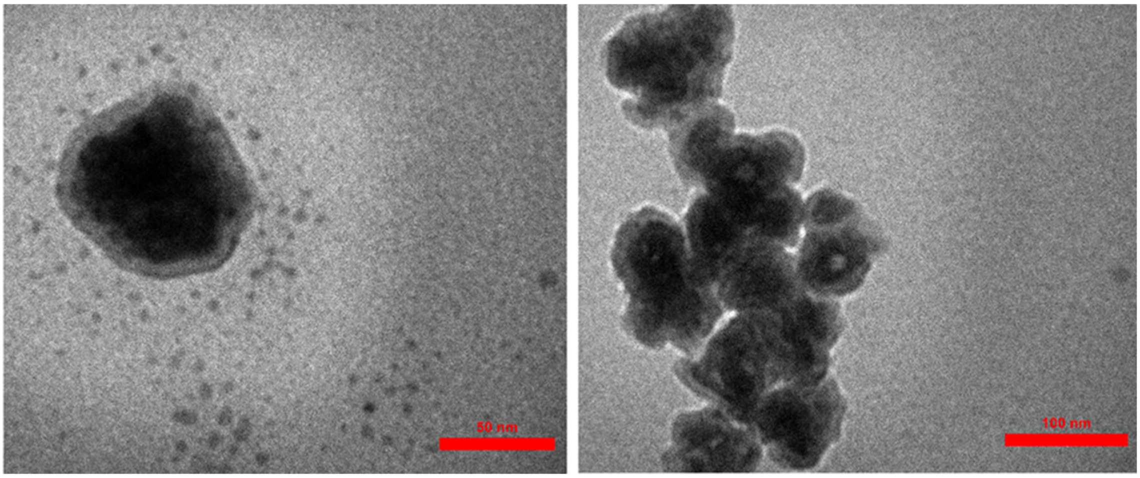

Fig. 8 The TEM images of $ZrFe_2O_4@SiO_2$-TCPP

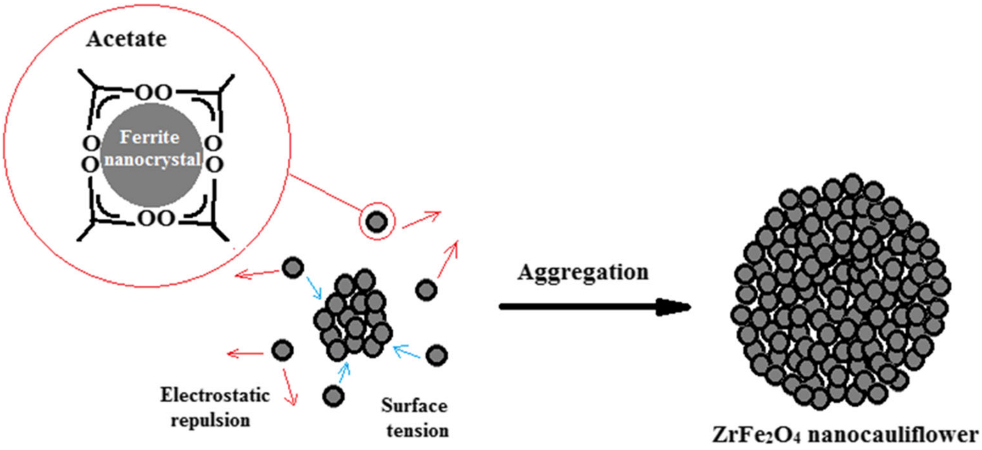

Fig. 9 Proposed mechanism for the formation of mesoporous Zr ferrite particles

using VSM in an external magnetic field ranging from −8 kOe to 8 kOe and compared with the coated material (SiO_2 and TCPP) as the shell which is synthesized, $ZrFe_2O_4$@SiO_2 and $ZrFe_2O_4$@SiO_2-TCPP (Fig. 12).

The saturation magnetization (Ms) value, extracted from the corresponding hysteresis loop, from the uncoated ferrite sample at 300 K is 18.3 emu/g. Ms. decreased for the coated samples as expected to be 12.4 and 5.7 emu/g for $ZrFe_2O_4$@SiO_2 and $ZrFe_2O_4$@SiO_2-TCPP, respectively, it demonstrates that SiO_2 and TCPP successfully wrapped $ZrFe_2O_4$ nanocauliflowers. By coating the silica on ferrite, the Fe ions tend to bond with silica (Fe-O-Si); thus, the magnetic moment of Fe ions would get diminished [55]. For the same reason, the

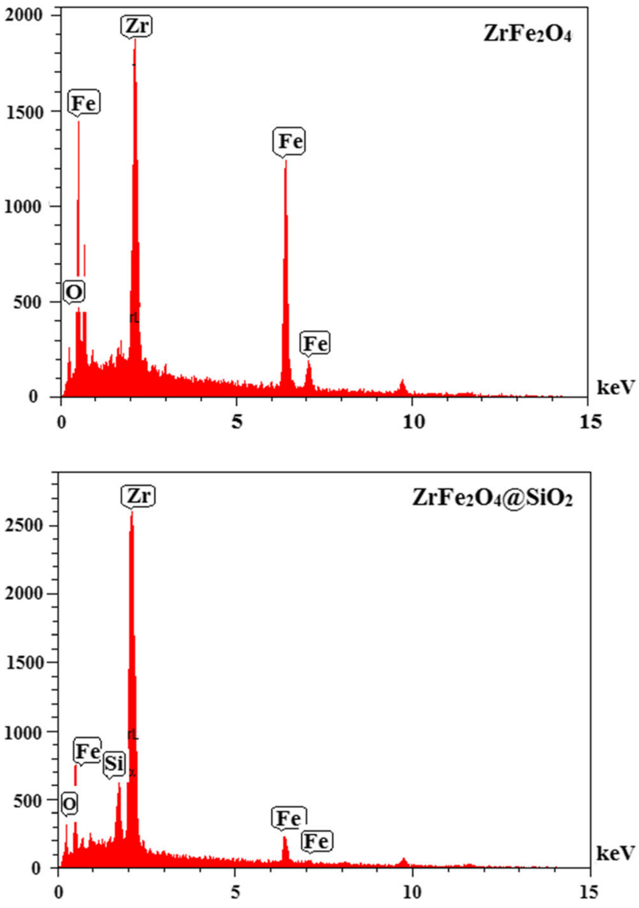

Fig. 10 The EDX analysis of $ZrFe_2O_4$ and $ZrFe_2O_4$@SiO_2

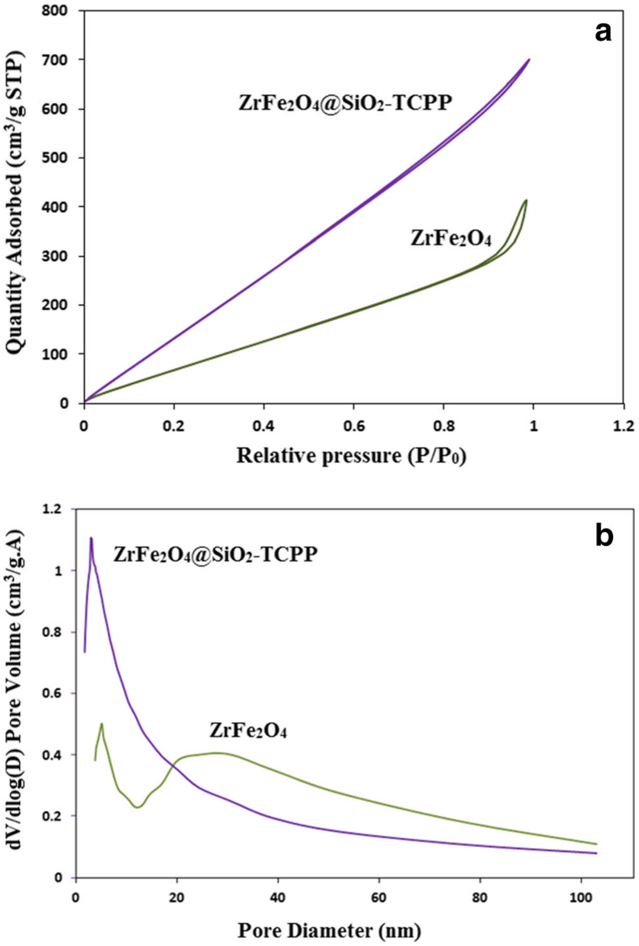

Fig. 11 **a** N_2 adsorption–desorption isotherms and (**b**) pore size distributions from the desorption branches through the BJH method of $ZrFe_2O_4$ and $ZrFe_2O_4$@SiO_2-TCPP

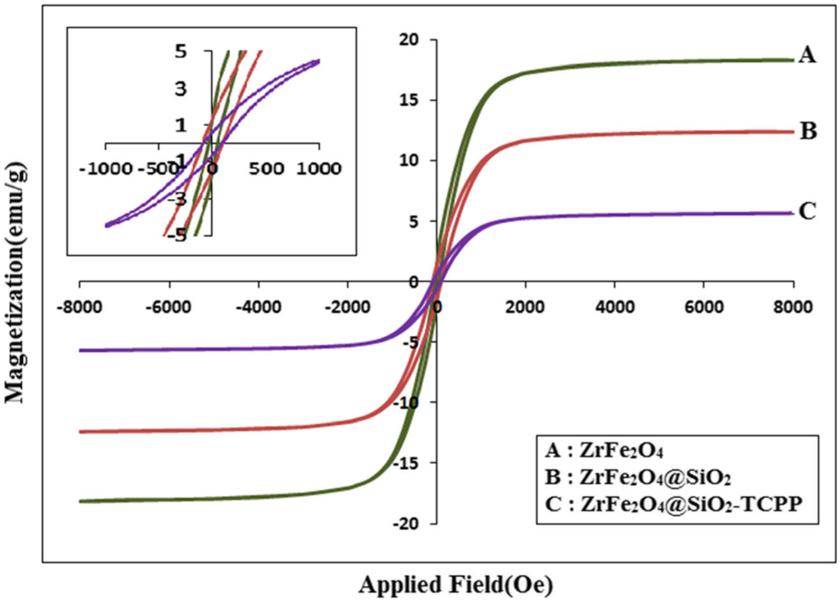

Fig. 12 The magnetization curves of the prepared samples

presence of TCPP causes a decrease in the magnetic properties of the nanomagnetic particles. However, their magnetic properties are still significant for the separation of these particles (as a catalyst) by using an external magnetic field [11].

The coercivity (Hc) values are little increased in the range of 50 Oe for the bare magnetite nanocauliflowers to 100 and 100 Oe for $ZrFe_2O_4@SiO_2$ and $ZrFe_2O_4@SiO_2$-TCPP respectively. This increasing can be occurred due to the shrinking of ferrite nanoparticles after immobilizing of SiO_2 and functionalizing with TCPP. The high coercivity of the nanoparticles could be caused by the magnetic moments of the nanoparticles, which are pined by the SiO_2, and TCPP. These evidences confirm the magnetic field direction as a result of single-domain nanoparticles [42, 56].

3.8 Fluorescence Spectra of the Prepared Samples

The fluorescence spectra of the prepared samples are shown in Fig. 13, providing more evidence to form the nanocomposite of $ZrFe_2O_4@SiO_2$-TCPP. The emission spectra of all prepared samples have shown emission peak at 430 nm (excitation peaks at 400 nm). After immobilizing TCPP on $ZrFe_2O_4@SiO_2$ nanocomposite ($ZrFe_2O_4@SiO_2$-TCPP), two peaks at 663 and 733 nm appeared which complied with peaks corresponded to pure TCPP. It predicts the binding of the porphyrin to the surface of nanocomposite [57].

3.9 Catalytic Study

The oxidation of cyclohexane in the liquid phase has been studied by $ZrFe_2O_4@SiO_2$-TCPP as catalysts (Scheme 2).

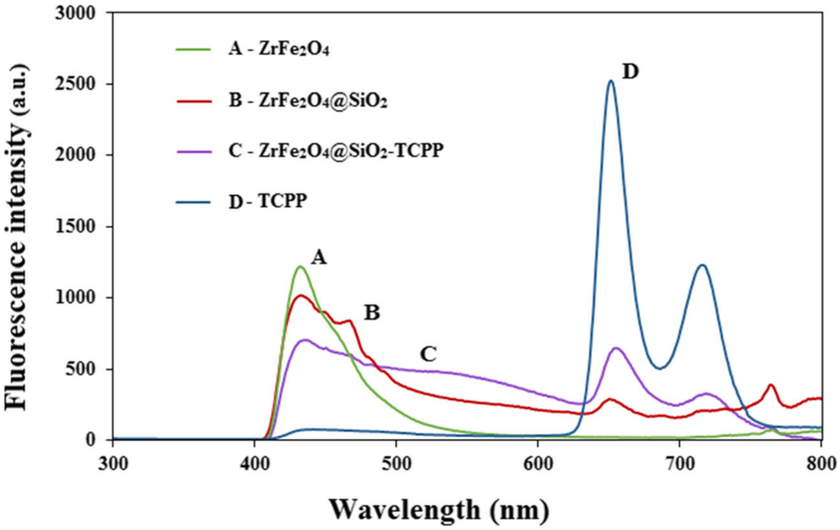

Fig. 13 The fluorescence of the prepared samples

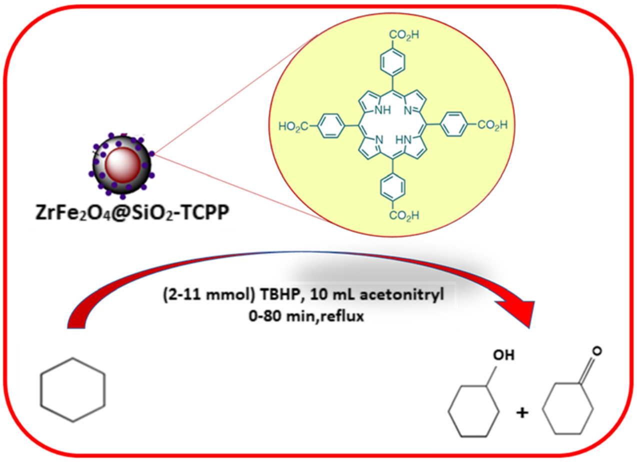

Scheme 2 The oxidation of cyclohexane by using $ZrFe_2O_4@SiO_2$-TCPP

Oxidation of cyclohexane was performed through initial experiments. The Central Composite Design (CCD) was used to optimize the reaction condition for the oxidation method. This approach will also be useful in economic terms. The 20 data analyses were performed using Design-Expert trial 7.0.0. Table 2 shows a reasonable range of each variable.

The statistical method used to optimize the three main operational variables, including $ZrFe_2O_4@SiO_2$-TCPP by w% as catalyst (A), TBHP by mmol as oxidant (B) and time of reaction by min (C) for maximum (Ke/Al) products. Accordingly, 20 experiments were determined by the modeling approach and the percentage of (Ke / Al) (Table 3).

By this method, to the analysis of variance (ANOVA) determines the adequacy of the model in addition to the significance and magnitude of the main effect and interaction of factors (See Tables 4, 5). A *p* value that is less than 0.05 in the ANOVA table showed the statistical significance of an effect at 95% confidence level. Also, F-value was applied to evaluate the statistical the significance of all terms in the polynomial equation at 95% confidence interval [34].

The model F-value of 7.9 for cyclohexanone and of 12.7 cyclohexanol indicates that the model is significant. The values ≥0.050 demonstrate that the model terms are not significant. For example, in the case of oxidation of cyclohexane, catalyst (A), oxidant (B) and time (C) interactions AB, AC, BC, A*2, B*2, C*2 are significant conditions of models.

Table 2 Experimental factors and levels with responses for oxidation of cyclohexane according to the Central Composite Design (CCD)

Code	Variable	Range				
		-1	0	+1	-α	+α
A	$ZrFe_2O_4@SiO_2$-TCPP (w%)	5	8	11	2	14
B	TBHP (mmol)	5	8	11	2	14
C	Time (min)	20	40	60	0	80

The lack of Fit (LOF) is the variety of data around the fitted model. The non-concurrence between the proposed model and experimental data is not favorable and makes the LOF significant [34]. According to our results (Tables 3, 4), the LOF of the *p* value for cyclohexanone and cyclohexanol are 0.2076 and 0.0937, respectively. These data demonstrate that LOF is not significant compared to the pure error that indicates the suitability of the model with the experimental data.

As following, based on the CCD method, a mutual relationship between the percentage of (Ke/Al) and independent variables of A, B and C were acquired:

$$Ke\% = 11.96 + 11.04\ \mathrm{A}–0.14\mathrm{B} + 3.11\mathrm{C} + 3.07\mathrm{B}^2$$

$$Al\% = 3.71 + 4.97\mathrm{A}–1.02\mathrm{B} + 1.16\mathrm{C}–2.04\mathrm{AB} + 1.45\mathrm{A}^2$$

3.9.1 Interaction of Operational Variables

The three-dimensional (3-D) curves were used to construe the interaction of operational variables. In 3-D plots, the simultaneous interaction of two variables on the response was evaluated, while the other two variables were constant at their center points.

Figure 14a-c show the interaction of three variables to produce the cyclohexanone (Ke), (a) shows the interaction between oxidant (mmol) and catalyst (w%). The low curvature of the graph showed the low impact of these two variables, so by increasing the amount of catalyst, the percentage of Ke will increase. However, the amount of mmoles of oxidant does not affect. (b) shows the interaction of time and catalyst (w%), while the other operational variable, including oxidant was kept constant at 11 mmol. The low curvature of the graph shows the low impact of these two variables according to the time chart, it has a little effect on the percentage of Ke, while the catalyst has a high effect on the percentage of it at 60 min and catalyst 11% the highest amount of Ke is obtained. In (c) The interaction of time and oxidant (mmol) is considered. The curvature of the graph shows the high impact of these two variables. The highest amount of Ke is obtained in the amount of oxidant 11 mmol and time of 60 min. In fact, by increasing the time and oxidant, the percentage of Ke production increases.

Figure 14d-f show these three variables to produce the cyclohexanol (Al). (d) The interaction between catalyst and oxidant is considered. Low curvature showed the low impact of these two variables, 5 mmol oxidant with 11% catalyst has the highest alcohol content. According to the graph, the amount of oxidant on the percentage of alcohol is negligible, while the percentage of the catalyst has a significant impact on the percentage of Al production. The effect of interaction with two variables of catalyst and time shows that the time has little impact on alcohol content, but the effect of catalysts in alcohol production is high, so the time in 60 min and

Table 3 Oxidation of cyclohexane by Central Composite Design (CCD)

Run[a]	$ZrFe_2O_4@SiO_2$-TCPP (w%)	Oxidant TBHP (mmol)	Time (min)	Cyclohexanone (mol%)	Cyclohexanole (mol%)	Conversion (mol%)[b]
1	8.00	8.00	40.00	10.2	3.32	6.14
2	5.00	11.00	60.00	0	0	0
3	8.00	8.00	40.00	16.71	3.53	6.01
4	8.00	8.00	40.00	9.92	5	4.21
5	5.00	5.00	20.00	0	0	0
6	11.00	5.00	20.00	25.3	14.5	8.09
7	5.00	5.00	60.00	0	0	0
8	11.00	5.00	60.00	32.2	14.5	9.00
9	8.00	8.00	0.00	8.34	4.29	5.08
10	14.00	8.00	40.00	30.2	18.9	12.54
11	8.00	8.00	40.00	9.64	2.43	4.95
12	8.00	8.00	80.00	25.54	7.23	4.43
13	5.00	11.00	20.00	0	0	0
14	11.00	11.00	20.00	25.1	0	4.04
15	8.00	8.00	40.00	10.1	4.21	3.41
16	2.00	8.00	40.00	0	0	0
17	8.00	14.00	40.00	23.9	0	4.13
18	8.00	2.00	40.00	25.6	0	2.99
19	11.00	11.00	60.00	33.6	12.65	15.63
20	8.00	8.00	40.00	1.94	6.74	2.20
21	–	11	60.00	0.6	0.5	0.3

[a] Reaction conditions: 10 mmol Cyc, 2–11% $ZrFe_2O_4@SiO_2$-TCPP, 5–11 mmol TBHP, 0–80 min and 10 mL acetonitrile by refluxing temperature.
[b] Conversions were calculated by resulting the GC-Mass

the catalyst in 11% produced the most amount of Al. Also, Fig. 14f considered the effect of the interaction of oxidant and time. Which indicates the great effect of these two variables on each other. So, the time is 60 min and the oxidant is 11 mmol have the most significant impact on Al production. Accordingly, it is essential to choose an optimum amount of variables to economize the oxidation process of cyclohexane.

Table 4 ANOVA for response surface quadratic model for cyclohexanone

Source	Sum of Squares	df	Mean Square	F – Value	p value Prob > F
Model	2473.13	9	274.79	7.90	0.0017 significant
A-cat	1949.22	1	1949.22	56.00	< 0.0001
B-oxidant	0.30	1	0.30	8.691E-003	0.9276
C-time	155.00	1	155.00	4.45	0.0610
AB	0.18	1	0.18	5.172E-003	0.9441
AC	29.64	1	29.64	0.85	0.3778
BC	0.32	1	0.32	9.194E-003	0.9255
A*2	32.98	1	32.98	0.95	0.3533
B*2	318.24	1	318.24	9.14	0.0128
C*2	64.79	1	64.79	1.86	0.2024
Residual	348.05	10	34.80		
Lack of Fit	238.24	5	47.65	2.17	0.2076 not significant
Pure Error	109.80	5	21.96		
Cor Total	2821.17	19			

$R^2 = 0.9816$, adjusted $R^2 = 0.9418$, predicted $R^2 = 0.8045$

Table 5 ANOVA for response surface quadratic model for cyclohexanol

Source	Sum of Squares	df	Mean Square	F – Value	P – value Prob > F
Model	600.09	9	66.68	12.70	0.0002 significant
A-cat	394.52	1	394.52	75.16	< 0.0001
B-oxidant	16.71	1	16.71	3.18	0.1047
C-time	21.46	1	21.46	4.09	0.0707
AB	33.42	1	33.42	6.37	0.0302
AC	20.00	1	20.00	3.81	0.0795
BC	20.00	1	20.00	3.81	0.0795
A*2	45.37	1	45.37	8.64	0.0148
B*2	26.12	1	26.12	4.98	0.0498
C*2	4.45	1	4.45	0.85	0.3788
Residual	52.49	10	5.25		
Lack of Fit	41.04	5	8.21	3.59	0.0937 not significant
Pure Error	11.45	5	2.29		
Cor Total	652.58	19			

$R^2 = 0.9542$, adjusted $R2 = 0.9341$, predicted $R2 = 0.8766$

3.9.2 Optimization and Confirmation

Optimization values obtained from RSM of the factors such as optimization of operational variables are of important due to the CCD model (Table 6). The "numerical optimization" was performed by setting response (Ke/Al (%)) to "maximum" level. The optimization result showed that the maximum Ke/Al product is equal to 18.9 and 33.6% with 52.5% selectivity.

3.9.3 Comparison to Other Catalysts

Table 7 shows the oxidation of cyclohexane by the other catalysts in comparison with $ZrFe_2O_4@SiO_2$-TCPP. In comparison, entry 6, 7 and 8 the oxidation of cyclohexane was performed by O_2 as oxidant which the selectivity of products (Ke/Al) were 25–85%, but the conversion of cyclohexane was not significant [32, 64]. In entry 3, TCPP(Fe) as the homogeneous

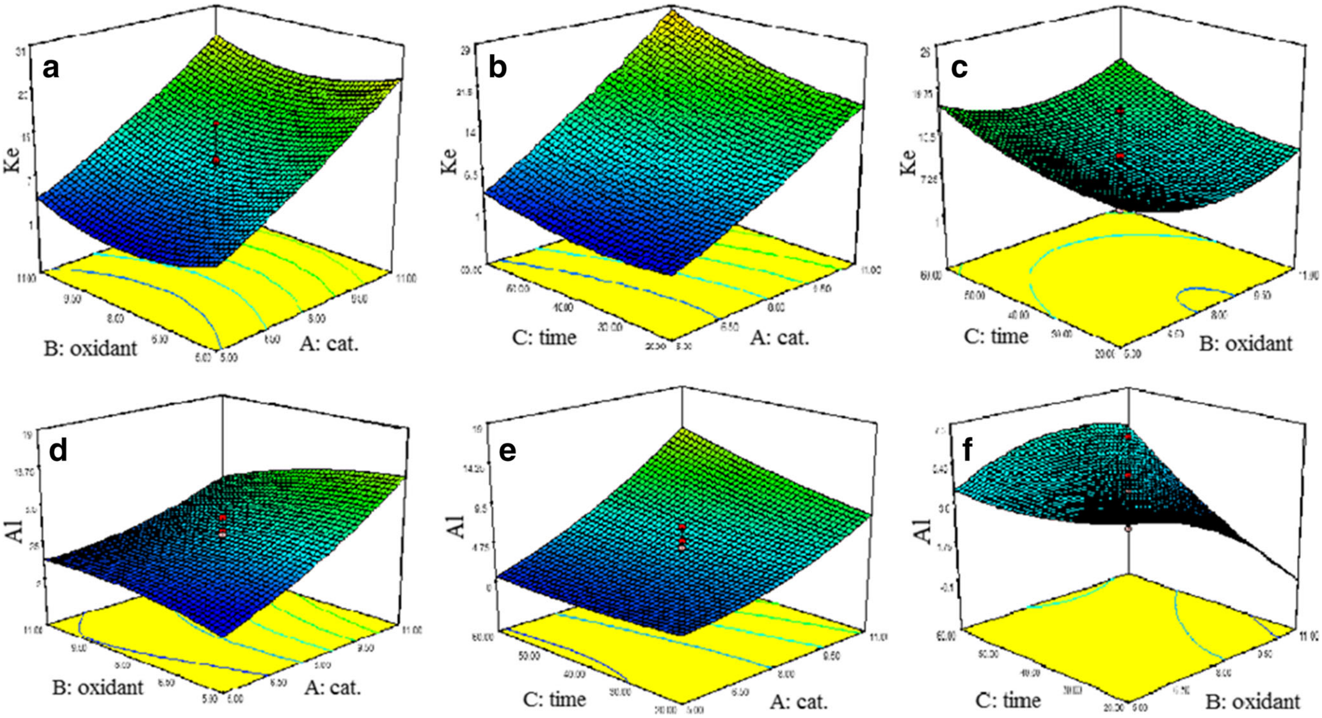

Fig. 14 The three-dimensional (3-D) curves of operational variables for Ke/Al

Table 6 Numerical optimization of variables (catalyst (A), oxidant (B) and time (C)) for Ke/Al

Optimal condition for responses (Ke-Al)	Variables
7.06–8.89	(A) Catalyst (w%)
11–11	(B) Oxidant (mmol)
60–60	Time (min)

catalyst by using TBHP as oxidant and mixture of CH_3CN and DMF as solvent was used. The Fe (III) located in the porphyrin center is indeed the active site for the reaction, but the conversion is low, this was happened due to the low solubility of TCPP in CH_3CN and surprisingly, the iron porphyrin is almost inactive under this condition, so the conversion of cyclohexane was low [58].

In this work the selectivity of the catalyst is 52.5% by the ratio of oxidant/catalyst, are 11 mmol/8 w% in optimal condition by DoE, and the conversion of cyclohexane is 15.63–12.54 mol%, easily removing by an external magnet from the reaction mixture is the substantial aspect of using this catalyst.

3.9.4 Reusability of the Nanocatalyst

This study shows that the catalyst can be used effectively for at least 5 times and isolated easily by an external magnet after the reaction. Figure 15 shows that there was no significant loss in catalytic activity and selectivity.

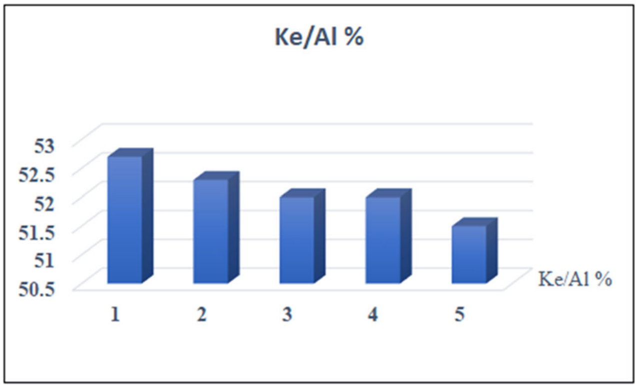

Fig. 15 Reusability study of the catalyst. Reaction conditions: cyclohexane 1.08 mL; TBHP 11 mmol $ZrFe_2O_4@SiO_2$- TCPP 9%; 10 mL acetonitrile; 60 min; in refluxing temperature

4 Conclusions

The result of XRD shows that the size of $ZrFe_2O_4$ has decreased by coating the SiO_2 and modifying with TCPP. Also, the wrapping of nanoparticles with SiO_2 and TCPP is appropriate to prevent the agglomeration of $ZrFe_2O_4$ nanoparticles. The BET results indicated that the nanocomposite with high specific surface area and narrow size distribution could be extended to synthesize mesoporous texture magnetic nanocomposites. The fabricated nanocomposite ($ZrFe_2O_4@SiO_2$-TCPP) is a suitable catalyst for oxidative reactions. Therefore, the transferring of electrons was easily done. Porphyrin provides the electron for the oxidation reaction. As well as, the advantages of this catalyst are easily removing by an external

Table 7 Comparison of the cyclohexane reaction by different catalysts

Entry	Catalyst	Conversion (mol%)	Ke – Al (mol%)	Reaction conditions	Ref.
1	$ZrFe_2O_4@SiO_2$-TCPP	–	52.5	Reaction based on the CCD method	This work
2	$[FeCl_2[HC(pz)_3]] + Fe_3O_4]$	0.5	4.8	Reaction conditions, unless stated otherwise: MeCN (3.0 mL), CyH (5.0 mmol), TBHP (70% aqueous solution,10.0 mmol), 2(10 mg), 50 °C, MW (5 W)	[13]
3	TCPP(Fe)	2<	–	Catalyst (10 mg), DMF (1 mL) and CH_3CN (1.5 mL). A mixture of CH_3CN and DMF was used due to the low solubility of TCPP in CH_3CN.	[58]
4	Manganeset (II) N, N-ethylene bis(salicylideneaminato)	10	22	Manganese (II) N,N-ethylene bis(salicylideneaminato) Mn complex (0.04 mmol), TBHP (4 mmol) and cyclohexane (40 mmol) were taken. Catalyst:oxidant:substrate molar ratio 1:100:1000. Reaction time 3 h. b Yield based on TBHP taken. Cyclohexanone yields were calculated considering the requirement of 2 mol of TBHP to produce 1 mol of ketone	[59]
5	CeY	–	1.58	Oxidation of cyclohexane with TBHP catalyzed by REY	[60]
6	Co-TPP	10.65	74.27	Cyclohexane 185 mmol, catalysts 1.8 mg, 155 °C for 1 h, oxygen pressure 1 Mpa	[61]
7	Co-SiO_2	6.0	85.7	Reaction was carried out with 0.12 g of catalyst and 0.12 g of TBHP in 15 g of cyclohexane at 388 K for 6 h under 1.0 Mpa O_2	[62]
8	Ag/Al_2O_3	2.7	25.4	Cyclohexane 0.1 mol, catalyst 0.042 g, O_2 1.4 Mpa, 413 K, stirrer, reaction time 3 h	[63]

magnet from the reaction medium, excellent reusability and suitable catalyst in oxidative reactions. Besides, the maximum selectivity of $ZrFe_2O_4@SiO_2$-TCPP as a catalyst by CCD optimization method for cyclohexanone and cyclohexanol products was respectively 33.6% and 18.9% by the amount of oxidant/catalyst, 11 mmol/8w% in 60 min. While the conversion of cyclohexane in the oxidation reaction was 12–16% under optimal condition by DoE.

Acknowledgements The authors gratefully acknowledge the partial support by Iran University of Science and Technology.

Compliance with Ethical Standards

Disclosure Statement No potential conflict of interest was reported by the authors.

References

1. Tong J, Cai X, Wang H, Xia C (2013) Efficient magnetic $CoFe_2O_4$ nanocrystal catalyst for aerobic oxidation of cyclohexane prepared by sol–gel auto-combustion method: effects of catalyst preparation parameters. J Sol-Gel Sci Technol 66:452–459
2. Davis DD, and Kemp DR, in "Kirk–Othmer (1991) Encyclopedia of Chemical Technology" (J. I. Kroschwitz and M. Howe-Grant, Eds.), 1: 466
3. Castellan A, Bart JCJ, Cavallaro S (1991) Industrial production and use of adipic acid. Catal Today 9:237–254
4. Dumas T, Bulani W (1974) Oxidation of petrochemicals: chemistry and technology. Applied Science, London, pp 53–64
5. Chavan SA, Srinivas D, Ratnasamy P (2002) Oxidation of cyclohexane, cyclohexanone, and cyclohexanol to adipic acid by a non HNO_3 route over Co/Mn cluster complexes. J Catal 212:39–45
6. Schuchardt U, Carvalho WA, Spinacé EV (1993) Why is it interesting to study cyclohexane oxidation? Synlett 10:713–718
7. Schuchardt U, Cardoso D, Sercheli R, Pereira R, Da Cruz RS, Guerreiro MC, Mandelli D, Spinacé EV, Pires EL (2001). Appl Catal A Gen 211:1–17
8. Suresh AK, Sharma MM, Sridhar T (2000) Engineering aspects of industrial liquid-phase air oxidation of hydrocarbons. Ind Eng Chem Res 39:3958–3997
9. Lang X, Chen X, Zhao J (2014) Heterogeneous visible light photocatalysis for selective organic transformations. Chem Soc Rev 43:473–486
10. Sideri IK, Voutyritsa E, Kokotos CG (2018) Photoorganocatalysis, small organic molecules and light in the service of organic synthesis: the awakening of a sleeping giant. Org Biomol Chem 16:4596–4614
11. Sankaranarayanapillai S, Sf V, Werner RT (2010) Magnetically separable nanocatalysts: bridges between homogeneous and heterogeneous catalysis. Angew Chem Int Ed 49:3428–3459
12. Ribeiro AP, Matias IA, Alegria EC, Ferraria AM, Botelho do Rego AM, Pombeiro AJ, Martins LM (2018) New trendy magnetic C-scorpionate iron catalyst and its performance towards cyclohexane oxidation. Catalysts 8:69
13. Maleki A, Hajizadeh Z (2019) Magnetic aluminosilicate nanoclay: a natural and efficient nanocatalystfor the green synthesis of 4H-Pyran derivatives. Silicon 11:2789–2798
14. Nabiyouni G, Ghanbari D, Ghasemi J, Yousofnejad A (2015) Microwave-assisted synthesis of $MgFe_2O_4$-ZnO nanocomposite and its photo-catalyst investigation in methyl orange degradation. J Nanostruct 5:289–295
15. Rahimi R, Kerdari H, Rabbani M, Shafiee M (2011) Synthesis, characterization and adsorbing properties of hollow Zn-Fe_2O_4 nanospheres on removal of Congo red from aqueous solution. Desalination 280:412–418
16. Jiang W, Zhang X, Gong X, Yan F, Zhang Z (2010) Sonochemical synthesis and characterization of magnetic separable Fe_3O_4–TiO_2 nanocomposites and their catalytic properties. Inter J Smart Nano Mater 1:278–287
17. Wu W, Xiao X, Zhang S, Ren F, Jiang C (2011) Facile method to synthesize magnetic iron oxides/TiO_2 hybrid nanoparticles and their photodegradation application of methylene blue. Nanoscale Res Lett 6:533
18. Soltani RDC, Mashayekhi M, Khataee A, Ghanadzadeh MJ, Sillanpää M (2018) Hybrid sonocatalysis/electrolysis process for intensified decomposition of amoxicillin in aqueous solution in the presence of magnesium oxide nanocatalyst. J Ind Eng Chem 64:373–382
19. Gangwar A, Alla S, Srivastava M, Meena S, Prasadrao E, Mandal R, Yusuf S, Prasad N (2016) Structural and magnetic characterization of Zr-substituted magnetite ($ZrxFe_{3-x}O_4$, $0\leq x\leq 1$). J Magn Magn Mater 401:559–566
20. Zhang L, Hp S, Zheng H, Lin T, Guo Z (2016) Synthesis and characterization of $Fe_3O_4@SiO_2$ magnetic composite nanoparticles by a one-pot process. Int J Miner Metall Mater 23:1112–1118
21. Hajizadeh Z, Maleki A, Rahimi R, Eivazzadeh-Keihan R (2019) Halloysite nanotubes modified by Fe_3O_4 nanoparticles and applied as a natural and efficient nanocatalyst for the symmetrical Hantzsch reaction. Silicon:1–10. https://doi.org/10.1007/s12633-019-00224-3
22. Maleki A, Kari T, Aghaei M (2017) $Fe_3O_4@SiO_2@TiO_2$-OSO_3H: an efficient hierarchical nanocatalyst for the organic quinazolines syntheses. J Porous Mater 24:1481–1496
23. Groves, JT, Shalyaev K, Lee J, Kadish KM, Smith KM, Guilard R (2000) The Porphyrin handbook, Eds. Academic Press 4: 17–40
24. Stephenson NA, Bell AT (2007) Effects of porphyrin composition on the activity and selectivity of the iron (III) porphyrin catalysts for the epoxidation of cyclooctene by hydrogen peroxide. J Mol Catal A Chem 272:108–117
25. Laybourn A, Dawson R, Clowes R, Hasell T, Cooper AI, Khimyak YZ, Adams DJ (2014) Network formation mechanisms in conjugated microporous polymers. Polym Chem 5:6325–6333
26. Monnereau C, Gomez J, Blart E, Odobel F (2005) Photoinduced electron transfer in platinum (II) terpyridinyl acetylide complexes connected to a porphyrin unit. Inorg Chem 44:4806–4817
27. Kira A, Umeyama T, Matano Y, Yoshida K, Isoda S, Park JK, Kim D, Imahori HJ (2009) Supramolecular donor−acceptor Heterojunctions by Vectorial stepwise assembly of Porphyrins and coordination-bonded fullerene arrays for photocurrent generation. Am Chem Soc 131:3198–3200
28. Liu CY, Bard A (1999) Optoelectronic properties and memories based on organic single-crystal thin films. J Acc Chem Res 32(3): 235–245
29. Fungo F, Otero L, Borsarelli CD, Durantini EN, SilberJJ SLJ (2002) Optoelectronic properties and memories based on organic single-crystal thin films. Phys Chem B 106:4070–4078
30. Gervaldo M, Fungo F, Durantini EN, Silber JJ, Sereno L, Otero L (2005) Carboxyphenyl metalloporphyrins as photosensitizers of semiconductor film electrodes. A study of the effect of different central metals. J Phys Chem B 109:20953–20962
31. Drain CM, Varotto A, Radivojevic I (2009) Self-organized porphyrinic materials. Chem Rev 109:1630–1658
32. Liu Q, Yang Y, Li H, Zhu R, Shao Q, Yang S, Xu J (2015) NiO nanoparticles modified with 5,10,15,20-tetrakis (4-carboxyl pheyl) porphyrin promising peroxidase mimetics for H_2O_2 and glucose detection. Biosens Bioelectron 64:147–153

33. Kathiravan A, Renganathan R (2009) Effect of anchoring group on the photosensitization of colloidal TiO_2 nanoparticles with porphyrins. J Colloid Interface Sci 331:401–407
34. Darvishi Cheshmeh Soltani R, Rezaee A, Khataee RA, Godini H (2014) Optimisation of the operational parameters during a biological nitrification process using response surface methodology. Can J Chem Eng 92:13–22
35. Shaykhi ZM, Zinatizadeh AAL (2014) Statistical modeling of photocatalytic degradation of synthetic amoxicillin wastewater (SAW) in an immobilized TiO_2 photocatalytic reactor using response surface methodology (RSM). J Taiwan Inst Chem Eng 45:1717–1726
36. Hassani A, Soltani RDC, Karaca S, Khataee A (2015) Preparation of montmorillonite–alginate nanobiocomposite for adsorption of a textile dye in aqueous phase: isotherm, kinetic and experimental design approaches. J Ind Eng Chem 21:1197–1207
37. Roosta M, Ghaedi M, Daneshfar A, Sahraei R, Asghari A (2015) Optimization of combined ultrasonic assisted/tin sulfide nanoparticle loaded on activated carbon removal of erythrosine by response surface methodology. J Ind Eng Chem 21:459–469
38. Weissman SA, Anderson NG (2015) Design of Experiments (DoE) and process optimization. Org Process Res Dev 19:1605–1633
39. Adler AD, Longo FR, Finarelli JD, Goldmacher J, Assour J, Korsakoff L (1967) A simplified synthesis for meso-tetraphenylporphine. J Organomet Chem 32:476–476
40. Li D, Dong W, Sun S, Shi Z, Feng S (2008) Photocatalytic degradation of acid chrome blue K with porphyrin-sensitized TiO_2 under visible light. J Phys Chem C 112:14878–14882
41. Wang W, Ma R, Wu Q, Wang C, Wang Z (2013) Magnetic microsphere-confined graphene for the extraction of polycyclic aromatic hydrocarbons from environmental water samples coupled with high performance liquid chromatography–fluorescence analysis. J Chromatogr A 1293:20–27
42. Rahimi R, Zargari S, Yousefi A, Berijani MY, Ghaffarinejad A, Morsali A (2015) Visible light photocatalytic disinfection of E. coli with TiO_2–graphene nanocomposite sensitized with tetrakis (4-carboxyphenyl) porphyrin. Appl Surf Sci 355:1098–1106
43. Yua J, Zhua S, Panga L, Chena P, Zhu GT (2018) Porphyrin-based magnetic nanocomposites for efficient extraction of polycyclic aromatic hydrocarbons from water samples. J Chromatogr A 1540:1–10
44. Bassiouk M, Basiuk VA, Basiuk EV, Álvarez-Zauco E, Martínez-Herrera M, Rojas-Aguilar A, Puente-Lee I (2013) Noncovalent functionalization of single-walled carbon nanotubes with porphyrins. Appl Surf Sci 275:168–177
45. Bosi F, Hålenius U, Skogby H (2009) Crystal chemistry of the magnetite-ulvospinel series. Am Min 94:181–189
46. Sorescu M, Xu T, Wise A, Díaz-Michelena M, McHenry ME (2012) Studies on structural, magnetic and thermal properties of $xFe_2TiO_{4\text{-}(1-\ x)}$ Fe_3O_4 ($0\leq\ x\leq\ 1$) pseudo-binary system. J Magn Magn Mater 324:1453–1462
47. Yan D, Xin J, Zhao Q, Gao K, Lu X, Wang G, Zhang S (2018) Fe-Zr-O catalyzed base-free aerobic oxidation of 5-HMF to 2,5-FDCA as a bio-based polyester monomer. Catal Sci Technol 8:164–175
48. Subramanian A, Annamalai A, Lee HH, Choi SH, Ryu J, Park JH, Jang JS (2016) Trade-off between Zr passivation and Sn doping on hematite nanorod photoanodes for efficient solar water oxidation: effects of a ZrO_2 underlayer and FTO deformation. ACS Appl Mater Interfaces 8:19428–19437
49. Luo JM, Luo XB, Hu CZ, Crittenden JC, Qu JC (2016) Zirconia (ZrO_2) embedded in carbon nanowires via electrospinning for efficient arsenic removal from water combined with DFT studies. ACS Appl Mater Interfaces 8:18912–18921
50. Kouotou PM, Vieker H, Tian ZY, Ngamou PHT, El Kasmi A, Beyer A, Golzhauser A, KohseHoinghaus K (2014) Structure activity relation of spinel type Co–Fe oxides for low-temperature CO oxidation. Catal Sci Technol 4:3359–3367
51. Nie JF, Liu HC (2014) Efficient aerobic oxidation of 5-hydroxymethylfurfural to 2, 5-diformylfuran on manganese oxide catalysts. J Catal 316:57–66
52. Deng H, Li X, Peng Q, Wang X, Chen J, Li Y (2005) Monodisperse magnetic single-crystal ferrite microspheres. Angew Chem 117: 2842–2845
53. Yu BY, Kwak SY (2011) Self-assembled mesoporous Co and Ni-ferrite spherical clusters consisting of spinel nanocrystals prepared using a template-free approach. Dalton Trans 40:9989–9998
54. Wang Y, Zhao H, Li M, Fan J, Zhao G (2014) Magnetic ordered mesoporous copper ferrite as a heterogeneous Fenton catalyst for the degradation of imidacloprid. Appl Catal B-Environ 147:534–545
55. Abbas M, Torati S, Lee C, Rinaldi C, Kim C (2014) Fe_3O_4/SiO_2 core/shell nanocubes: novel coating approach with tunable silica thickness and enhancement in stability and biocompatibility. J Nanomed Nanotechnol 5:1–8
56. Issa B, Obaidat I, Albiss B, Haik Y (2013) Magnetic nanoparticles: surface effects and properties related to biomedicine applications. Int J Mol Sci 14:21266–21305
57. Sun L, Li Y, Sun M, Wang H, Xu S, Zhang C, Yang Q (2011) Porphyrin-functionalized $Fe_3O_4@SiO_2$ core/shell magnetic colorimetric material for detection, adsorption and removal of Hg^{2+} in aqueous solution. New J Chem 35:2697–2270
58. Li L, Yang Q, Chen S, Hou X, Liu B, Lua J, Jiang H-L (2017) Boosting selective oxidation of cyclohexane over a metal–organic framework by hydrophobicity engineering of pore walls. Chem Commun 53(72):10026–10029
59. Bezaatpour A, Khatami S, Nejati K (2017) Cis-dioxo-Mo (VI) salophen complex supported on $Fe_3O_4@SiO_2$ nanoparticles as an efficient magnetically separable and reusable nanocatalyst for selective epoxidation of olefins. J Iran Chem Soc 14(10):2105–2115
60. Pires E-L, Wallau M, Schuchardt U (1997) Selective oxidation of cyclohexane over rare earth exchanged zeolite Y. Stud Surf Sci Catal 110:1025–1027
61. Xie Y, Zhang F, Liu P, Hao F, Luo H (2013) Synthesis and catalytic properties of trans-A_2B_2-type metalloporphyrins in cyclohexane oxidation. Can J Chem 92(1):49–53
62. Zhang Q, Chen C, Wang M, Cai J, Xu J, Xia C (2011) Facile preparation of highly-dispersed cobalt-silicon mixed oxide nanosphere and its catalytic application in cyclohexane selective oxidation. Nanoscale Res Lett 6(1):586
63. Zhao H, Zhou J, Luo H, Zen C (2006) Synthesis, characterization of Ag/MCM-41 and the catalytic performance for liquid-phase oxidation of cyclohexane. Catal Lett 108:1–2
64. Maleki A, Aghaei M, Hafizi-Atabak H-R, Ferdowsi M (2017) Ultrasonic treatment of $CoFe_2O_4@B_2O_3\text{-}SiO_2$ as a new hybrid magnetic composite nanostructure and catalytic application in the synthesis of dihydroquinazolinones. Ultrason Sonochem 37:260–266